scientific reports

Check for updates

OPEN

Paired regional complementarity in diffusion MRI reveals disease-specific microstructural profiles in PD, MSA, and PSP: a feasibility study

Abel Worku Tessema[1,2,7], Sungyang Jo[3,7], Young Ro Kim[4], Hyoyoung Lee[3], Grace Yoojin Lee[5], Chong Hyun Suh[6], Jihong Ryu[3], Sun Ju Chung[3], Eun-Jae Lee[3]✉ & HyungJoon Cho[1]✉

Parkinson's disease (PD) is a prevalent neurodegenerative disorder characterized by tremor, rigidity, bradykinesia, and postural instability. Atypical Parkinsonian syndromes such as progressive supranuclear palsy (PSP) and multiple system atrophy (MSA) share overlapping clinical features, complicating accurate diagnosis. While prior diffusion MRI studies have used large, opaque machine-learning models, this study explored the best two diffusion metrics to differentiate Parkinsonian syndromes. This strategy introduces a compact and interpretable approach tailored for clinically relevant cohort sizes. We retrospectively analyzed diffusion MRI data from 199 patients (PD: 140, PSP: 20, MSA: 39) and constructed age- and sex-matched subsets comprising 40 PD, 20 PSP, and 34 MSA subjects to ensure controlled and balanced group comparisons. Mean diffusivity (MD) and fractional anisotropy (FA) were extracted from twelve predefined brain regions. Deformation-based morphometry and deterministic tractography were also used to map macrostructural and pathway-specific changes. Statistical comparisons and logistic regression with cross-validation assessed discriminatory power. MSA patients exhibited significant atrophy, increased MD, and decreased FA in the cerebellum. PSP showed pronounced changes in the superior cerebellar peduncle and corpus callosum. Putamen, corpus callosum, and cerebellum emerged as key discriminators for PD, PSP, and MSA, respectively. A compact and strategically selected set of diffusion features significantly improved disease differentiation. This study demonstrates that interpretable, region-specific complementarily paired diffusion patterns can robustly distinguish PD, PSP, and MSA, offering a transparent and biologically meaningful framework for differential diagnosis and mechanistic understanding.

Keywords Parkinsonian syndromes, Diffusion tensor imaging, Tractography, Differential diagnosis

Abbreviations

AD	Axial diffusivity
AUC	Area under the curve
CC	Corpus callosum
CWM	Cerebellar white matter
DBM	Deformation-based morphometry
DTI	Diffusion tensor imaging

[1]Department of Biomedical Engineering, Ulsan National Institute of Science and Technology, 105-222, 50, UNIST-gil, Eonyang-eup, Ulju-gun, Ulsan, Republic of Korea. [2]School of Biomedical Engineering, Jimma Institute of Technology, Jimma University, Jimma, Ethiopia. [3]Department of Neurology, Asan Medical Center, Seoul, Republic of Korea. [4]Athinoula A. Martinos Center for Biomedical Imaging, Department of Radiology, Massachusetts General Hospital, Charlestown, MA, USA. [5]Department of Medical Science, Asan Medical Institute of Convergence Science and Technology, Asan Medical Center, University of Ulsan College of Medicine, Seoul, Republic of Korea. [6]Department of Radiology and Research Institute of Radiology, Asan Medical Center, University of Ulsan College of Medicine, Seoul, Republic of Korea. [7]Abel Worku Tessema and Sungyang Jo contributed equally to this work. ✉email: eunjae.lee@amc.seoul.kr; hjcho@unist.ac.kr

FA	Fractional anisotropy
FD	Fiber density
GQI	Generalized Q-sampling imaging
ICBM152	International Consortium for Brain Mapping 152
ICV	Intracranial volume
MCP	Middle cerebellar peduncle
MD	Mean diffusivity
MRI	Magnetic resonance imaging
MSA	Multiple system atrophy
PCA	Principal Component Analysis
PCs	Principal components
PD	Parkinson's disease
PSP	Progressive supranuclear palsy
RD	Radial diffusivity
ROC	Receiver operating characteristic
SCP	Superior cerebellar peduncle
SN	Substantia nigra
TE	Time of echo
TR	Time of repetition

Parkinson's disease is a neurological disorder mainly characterized by clinical symptoms, including bradykinesia, rigidity, resting tremor, postural instability, cognitive decline, loss of memory and coordination, as well as behavioral changes[1,2]. Patients with atypical Parkinsonism, including progressive supranuclear palsy (PSP) and multiple system atrophy (MSA), often present with overlapping clinical symptoms with PD patients, making accurate diagnosis challenging[2–4]. PD is distinguished mainly by the loss of dopaminergic neurons, which control body movements and behavior in the substantia nigra (SN), leading to dopamine depletion and motor symptoms[5]. PSP is the most common atypical Parkinsonian syndrome, which is caused by the accumulation of tau protein or tauopathy in different brain regions, such as the basal ganglia, leading to dysfunction in motor control, eye movement, and cognition, and is highly susceptible to misdiagnosis as PD due to its Parkinsonian features[6–9]. In addition to its Parkinsonian features, PSP also shows atrophy of midbrain structures such as the SN[9,10]. MSA is another atypical Parkinsonian syndrome, often characterized by the accumulation of alpha-synuclein, or synucleinopathy, in oligodendrocytes, resulting in widespread neurodegeneration in the basal ganglia, cerebellum, brainstem, and other areas[11,12]. It is classified into Parkinsonian (MSA-P) and cerebellar (MSA-C) subtypes. MSA-P has clinical features that mostly overlap with PD, while MSA-C has other features, such as cerebellar ataxia[12].

Most of the clinical symptoms of PD, PSP, and MSA overlap across all stages of the disease, and accurately differentiating one from the other for effective medical treatment remains clinically challenging[2–4,13–15]. Currently, magnetic resonance imaging (MRI) is utilized in a variety of neuroscience studies due to its high sensitivity to a wide range of structural, diffusion, and metabolic changes, which can help us study and evaluate brain function[3,8,16–18]. In addition to conventional structural MRI, neuromelanin-sensitive MRI, susceptibility-weighted imaging, quantitative susceptibility mapping, as well as diffusion MRI, are commonly used for the study and diagnosis of Parkinsonism[19–21]. Using structural MRI data, many researchers have found morphological changes in different brain tissues, which may serve as a biomarker for differentiating Parkinsonian syndromes[10,22]. Severe midbrain atrophy, with the characteristic "hummingbird" sign, as well as thinning of the corpus callosum (CC), are the most commonly identified morphological indicators for differentiating PSP[23–26]. In addition, atrophy of the pons, putamen, and cerebellum are mostly known indicators of MSA, while PD patients typically experience less tissue morphological changes compared to PSP and MSA[22,26]. Using iron-sensitive MRI, accumulation of iron in SN, putamen, and other midbrain structures is used to differentiate PD, MSA, and PSP[27].

In recent years, diffusion tensor imaging (DTI), an advanced MRI technique, has gained significant attention for its ability to use diffusion-weighted data acquired from multiple orientations to formulate a diffusion tensor[3,28,29]. This diffusion tensor characterizes the overall behavior of water diffusion in tissue, including its magnitude and orientation, making it a valuable tool for studying changes in tissue microstructure and its association with various neurological conditions[28,29]. The key DTI-driven metrics, such as mean diffusivity (MD), fractional anisotropy (FA), axial diffusivity (AD), as well as radial diffusivity (RD), can be utilized to differentiate PD, PSP, and MSA[3,5,24,30]. MD measures the overall water diffusivity, with an increase in MD often linked to neurodegeneration, as the space previously occupied by neurons becomes filled with mostly free water[5,31]. FA quantifies the directionality of water diffusion, reflecting the integrity of neuronal bundles, and a lower FA mostly indicates neurodegeneration and demyelination[5,31]. In addition, AD and RD help us to differentiate changes in water diffusion due to axonal loss or demyelination, respectively[5,31]. Diffusion metrics of certain brain regions have shown promising results in differentiating various Parkinsonian syndromes. Regional variations in diffusion MRI metrics, particularly MD and FA values, in brain regions such as the putamen, cerebellar white matter (CWM), CC, pons, middle cerebellar peduncle (MCP), superior cerebellar peduncle (SCP), thalamus, globus pallidus, caudate nucleus, and others have been consistently reported as biomarkers for differentiating PD, PSP, and MSA[32–34]. DTI-based fiber tractography, which makes tracking neural bundles possible, can also help us investigate neuronal damage and brain connectivity[29]. Since neurodegenerative disease induces neuronal loss, tractography can also lead us to quantify fiber density (FD), providing valuable insights about the degree of white matter disruption and allowing for early detection and monitoring of disease progression[33]. Tractography of neuronal pathways such as the MCP, SCP, olfactory, callosal, and nigrostriatal

pathways, among others, has also served as a pathological biomarker for differentiating Parkinsonian syndromes as well[5,8,35–38].

Despite substantial progress using large-cohort machine-learning studies that optimize classification accuracy using DTI[3], few have clarified how spatially heterogeneous diffusion abnormalities collectively distinguish PD, PSP, and MSA groups. This gap is particularly critical for small, clinically relevant cohorts, where limited sample sizes and the need for interpretability regardless of disease duration constrain the utility of black-box models. Diffusion alterations in PD, PSP, and MSA are both pathway-specific and spatially distributed, therefore, relying on a single metric such as MD or FA from a single region can obscure diagnostically meaningful patterns. Instead of developing another high-dimensional classifier, we systematically integrate complementarily paired diffusion metrics across key brain regions to uncover distinct disease-specific microstructural signatures. By mapping whole-brain morphological and microstructural changes, we identify the most informative biomarkers and show how complementarily paired regional diffusion metrics, such as low FA of MCP combined with high FA of putamen, enhance differentiation of PD versus MSA. Our objective is to delineate the diffusion features that mechanistically distinguish PD, PSP, and MSA subtypes, thereby illuminating disease-specific patterns of structural deformation and pathway degeneration through an interpretable framework designed for modest-sized cohorts and easily translatable to routine clinical applications without reliance on black-box models.

Methods

In vivo MRI

This study utilized retrospective data from patients diagnosed with Parkinsonism at Asan Medical Center (Seoul, Republic of Korea) between January 2022 and December 2023. The DTI data was collected using a repetition time (TR) of 4000 ms, echo time (TE) of 78 ms, resolution of (1.75×1.75) mm^2, slice thickness of 2 mm, flip angle of 90°, and matrix size of $(128 \times 128 \times 70)$ using a 2D axial acquisition scheme. In addition, the b-value and number of diffusion directions were set to 1000 s/mm^2 and 64, respectively, and a single b_0 image was acquired. The data was acquired using a 3 T Philips MRI scanner (Philips, the Netherlands) equipped with a multi-channel array head coil. The study protocol was approved by the Institutional Review Board (Approval number 2024-0099) of Asan Medical Center. Informed consent was obtained from all participants, and all procedures were conducted in accordance with the Declaration of Helsinki. In addition, all data were anonymized to ensure patient confidentiality. Patients were diagnosed by two experienced neurologists with 20 and 10 years of experience in movement disorders using the UK Brain Bank criteria for PD[39], probable MSA consensus diagnostic criteria[40], and probable PSP criteria[41]. In this research, DTI data from 140 PD, 20 PSP, and 39 MSA patients were used. For comparison of PD, PSP, and MSA groups, age- and gender-matched data from 40 PD, 20 PSP, and 34 MSA patients were utilized. Among the 34 MSA patients, 10 were diagnosed as MSA-P, 10 as MSA-C, and the remaining 14 patients as unclassified. In addition, to compare MSA subtypes, age and gender balanced cohort consisting of 13 MSA-C and 12 MSA-P patients was also studied.

Data registration

First, to create a native PD template, b_0 images of separate 100 PD patients' data were aligned using non-linear registration and averaged, followed by manual masking to exclude non-brain regions of the template. Figure 1 demonstrates the overall workflow of the analysis. All patients' diffusion data were then non-linearly registered to the native PD template, and the corresponding b-vectors were also corrected by using the rotation matrix during image registration. Each subject's brain mask was obtained by applying the inverse transformation of the template mask, and the intracranial volume (ICV) was subsequently estimated. Deformation-based morphometry (DBM), based on the Jacobian determinant, was also determined to evaluate local structural deformations of brain tissues. After aligning all data, group-wise average DTI data was also generated by averaging all 4D data in each disease group.

DTI data processing

Diffusion metrics such as MD, AD, RD, and FA were extracted using diffusion imaging in Python (DIPY) (version: 1.9.0, available at: https://dipy.org/) from aligned DTI data. In addition, the FD map was also extracted using DSI Studio (version: Chen, available at: https://dsi-studio.labsolver.org/) after performing whole brain tractography using quantitative anisotropy as the tracking metric. Diffusion data were reconstructed using generalized q-sampling imaging (GQI), which estimates the spin distribution function from multiple diffusion-weighted images[42]. GQI can resolve multiple and complex fiber orientations, such as fiber crossings, which were difficult to resolve in conventional DTI reconstruction[42,43]. GQI reconstruction was performed using a diffusion sampling length ratio of 1.25, and tensor metrics were calculated from DWI data with b-values less than 1750 s/mm^2. Deterministic whole-brain tractography was also performed with a minimum streamline length of 30 mm, a maximum length of 200 mm, topology-informed pruning set to 4, an auto tolerance of 24 mm, and a seeding of one million[44,45]. In addition, specific neuronal pathways, including the corpus callosal, MCP, and SCP pathways, were extracted using auto-tracking of DSI studio followed by manual correction to remove unrelated streamlines using the group-wise average DTI data. The streamlines were then visually evaluated and compared across the disease groups.

Region-based analysis

To explore and identify sensitive brain tissues and diffusion metrics that can be a better biomarker to differentiate Parkinsonian syndromes, five diffusion metrics (AD, FA, AD, RD, and FD) were extracted from twelve brain tissues. Tissue masks were generated in DSI Studio by non-linearly registering the group averaged DTI data to the International Consortium for Brain Mapping 152 (ICBM152) brain template[46]. A total of 60 DTI features were extracted from each subject. Since each diffusion metric had a different range, the data were then

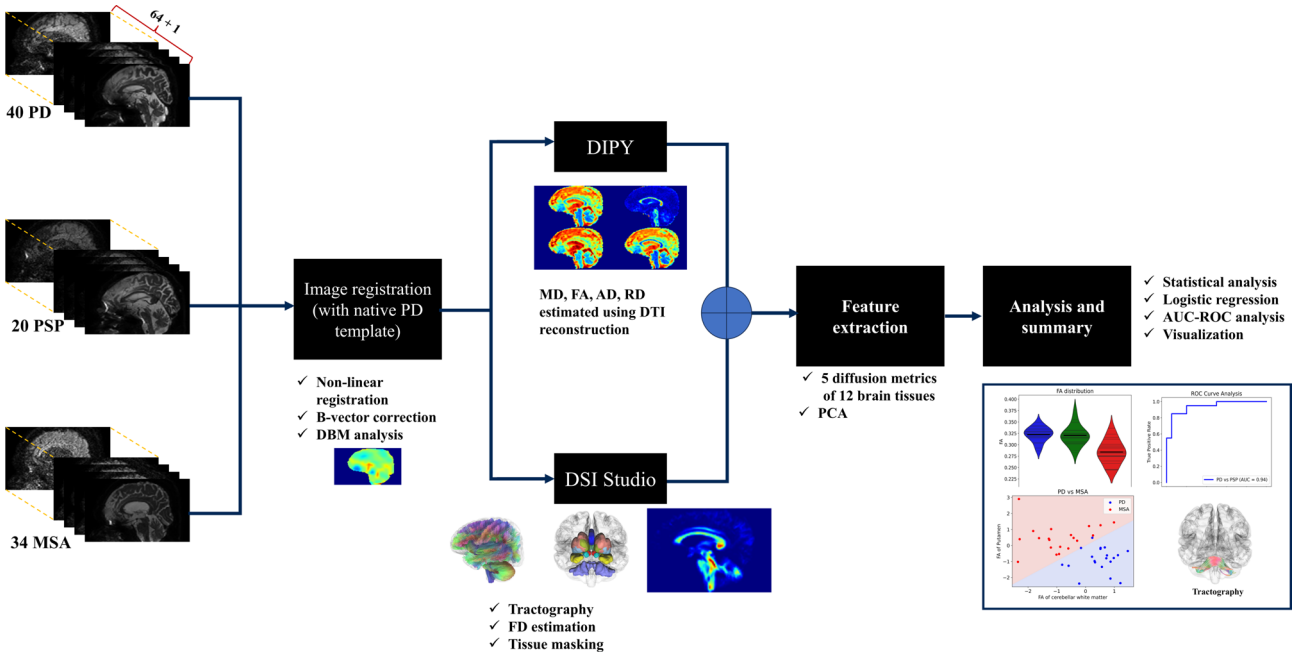

Fig. 1. A general block diagram illustrating the overall workflow of the proposed framework for differentiating Parkinsonian syndromes using diffusion data.

standardized. After extracting the metrics, a rigorous exploration was performed to choose a combination of two complementarily paired diffusion metrics of selected tissues that provides maximum differentiating power for each disease pair. The differentiability of the classes was evaluated using logistic regression and area under the curve (AUC) of the receiver operating characteristic (ROC) curve, with four-fold cross-validation to ensure that test datasets remained independent from training data. In addition, to account for overlapping clinical features among the disease groups and to enable direct comparison with differentiation using two complementary metrics, we assessed class separability using multiple diffusion metrics transformed into orthogonal features through principal component analysis (PCA). PCA was employed for dimensionality reduction and feature prioritization, using scikit-learn (version: 1.6.1, available at: https://scikit-learn.org/). The number of principal components (PCs) was optimized to maximize classification performance while minimizing the risk of overfitting in logistic regression. Accordingly, the first seven PCs were used as input for multivariable logistic regression with L_2 regularization and a balanced loss to assess the ability to differentiate between disease groups with four-fold cross-validation.

Statistical analysis

Basic patient information, including age, gender, and ICV, was compared among the three groups using the Kruskal–Wallis H test and the Mann–Whitney U test. Diffusion metric maps were extracted, and voxel-wise statistical comparisons between groups were conducted using the Mann–Whitney U test. We used an uncorrected p-value of 0.01 considering the exploratory nature of this study and the relatively small sample size. This method reduces the probability of spurious voxel-wise findings while retaining larger, spatially coherent clusters that are more likely to reflect meaningful effects. For group comparisons based on the mean diffusion metrics of selected brain tissues, the Kruskal–Wallis H test followed by the Mann–Whitney U test with Bonferroni post hoc correction was employed. ROC curve analysis was conducted to calculate the AUC, assessing the overall ability to distinguish between groups using various combinations of diffusion metrics. Statistical significance thresholds were set at $p < 0.05$ for the Kruskal–Wallis H test and $p < 0.0083$ (0.05/6) for the Mann–Whitney U test with Bonferroni correction, taking into account the six pairwise comparisons including MSA subtypes.

Results

Basic patient information is summarized in Table 1. The analysis showed no statistically significant differences in age, gender, ICV, or whole brain tractography between the PD, PSP, and MSA groups (all $p > 0.4$). Furthermore, no statistically significant differences were found in age, gender, or ICV between the MSA-P and MSA-C groups (all $p > 0.5$).

When comparing the disease groups using voxel-wise statistical analysis of DBM maps, MSA patients experience atrophy mainly in CWM and pons compared to PD patients as shown in Fig. 2. In addition, PSP patients also show atrophies of different brain regions compared to PD and MSA patients. To better illustrate the results of the voxel-wise statistical analysis, pairs of the axial, coronal, and sagittal slices from different brain positions are visualized, as shown in Figs. 2 and 3.

Basic information	PD (N = 40)	PSP (N = 20)	MSA (N = 34)	Kruskal–Wallis		Post hoc (*p*)		
				χ^2	*P*	PD *vs.* PSP	PD *vs.* MSA	PSP *vs.* MSA
Gender	21 M/19F	12 M/8F	18 M/16F	0.34	0.86	0.60	0.98	0.63
Age	66.9 ± 7.6	68.5 ± 5.6	66.5 ± 6.2	1.04	0.60	0.64	0.64	0.26
ICV in cm^3	1350 ± 123	1328 ± 135	1339 ± 142	0.49	0.78	0.51	0.63	0.87
Whole brain tractography	466,833 ± 28,459	449,780 ± 23,939	460,026 ± 24,320	6.84	**0.03***	0.013	0.32	0.06

Table 1. Statistical analysis of basic patient information. Data are shown as mean ± standard deviation. *: $p < 0.05$. The significant *p*-values are displayed in bold.

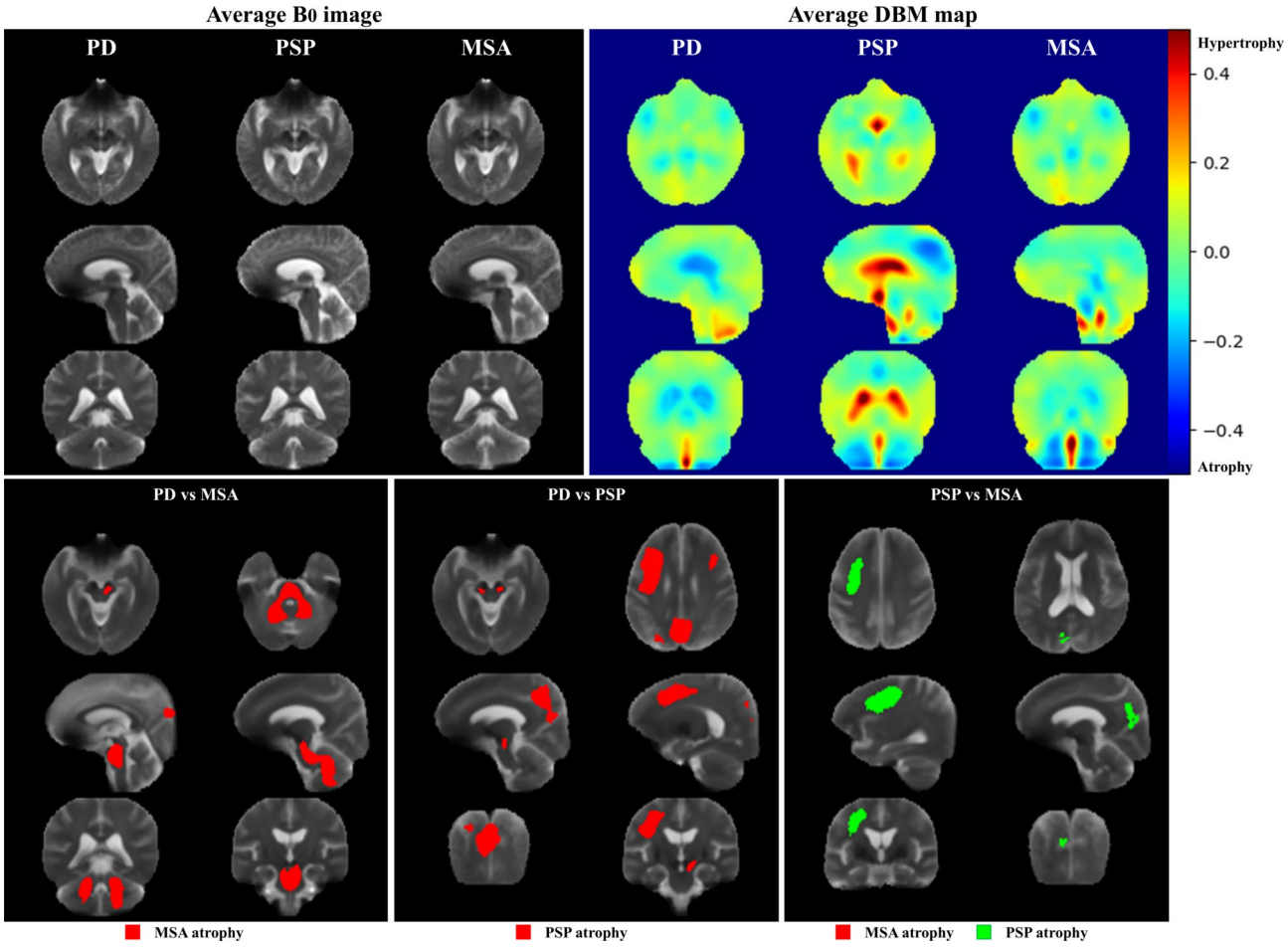

Fig. 2. Voxel-wise DBM analysis comparing structural deformations among PD, PSP, and MSA groups. To retain meaningful 3D clusters, a voxel-wise threshold of $p < 0.01$ was applied, along with a connectivity criterion requiring a minimum cluster size of 10 contiguous voxels.

Voxel-wise statistical analysis of MD and FA maps comparing PD, PSP, and MSA groups revealed that MSA patients exhibit higher MD and lower FA in the pons and CWM compared to PD, as shown by the highlighted and clustered voxels with statistically significant changes in Fig. 3. PSP patients show higher MD and lower FA mainly in CC compared to both PD and MSA groups. When comparing the two MSA subtypes, the MSA-C type showed higher MD and lower FA in the pons and CWM compared to the MSA-P type, as shown in Fig. 3.

Comparing the disease classes using the diffusion metrics of twelve different brain regions, as shown in Table 2 and Supplementary Tables 1, reveals that diffusion metrics of some brain tissues have high distinguishing power for each disease type. Figure 4 summarizes which brain tissue and diffusion metrics have high distinguishing power for each disease group. There was significantly lower (both *p* values $< 10^{-4}$) FA of CWM in MSA patients compared with PD and PSP. There was also significantly reduced FA of CC in PSP patients (both *p* values < 0.0002) compared with PD and MSA. PD patients show significantly lower FA of the putamen ($p = 0.0014$ and $p < 10^{-4}$), compared with PSP and MSA respectively. In addition, MSA-P patients show significantly higher MD in the

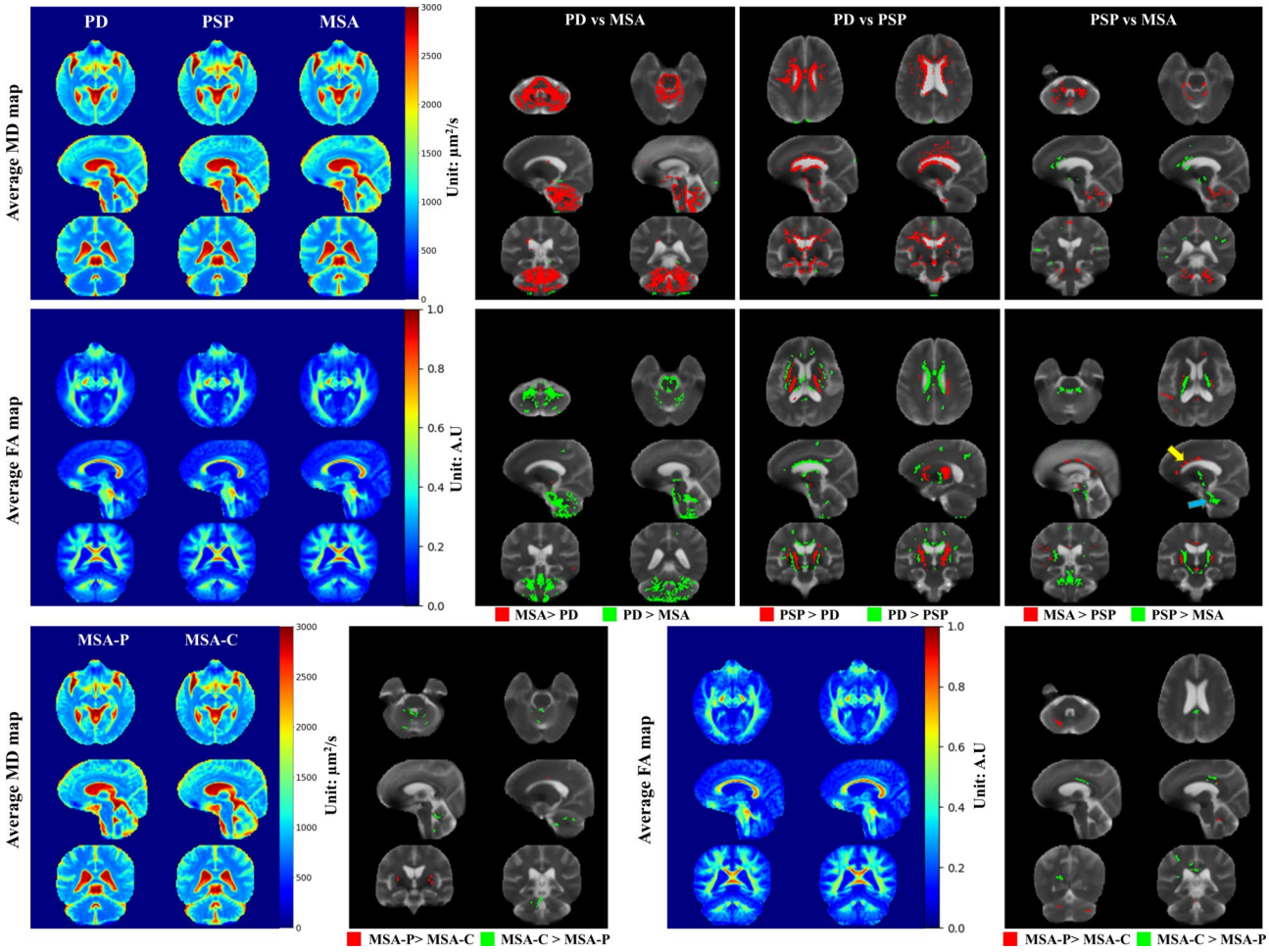

Fig. 3. Voxel-wise statistical analysis using MD and FA comparing PD, PSP, and MSA groups, including MSA subtypes. Highlighted voxels show significant differences ($P < 0.01$) combined with a connectivity criterion requiring a minimum cluster size of 10 contiguous voxels. The yellow and blue arrows highlight examples of the complementary roles of FA in the CC and CWM, respectively, in distinguishing the PSP and MSA groups.

putamen ($p = 0.003$) compared to MSA-C type. MSA-C patients show significantly higher MD and lower FA in the CWM (both p values $< 10^{-4}$) compared to PD.

When comparing the disease groups using whole brain tractography, PSP patients exhibited fewer streamlines than the other groups, although the difference in total streamline count was not statistically significant, as shown in Table 1 and Supplementary Fig. 1. Furthermore, voxel-wise statistical analysis of the FD map revealed that MSA patients had significantly fewer streamlines in the CWM and pons compared to PD, while PSP patients showed a marked reduction in streamlines primarily within the CC, as illustrated in Supplementary Fig. 1. Region-wise statistical analysis of the FD map further indicated that PD patients exhibited a significantly lower number of streamlines in the putamen and striatum (all p values < 0.002) compared to both PSP and MSA, as shown in Supplementary Table 1.

Furthermore, using tractography from group-wise average DTI data, PSP patients exhibit fewer streamlines across CC, which may reflect degeneration of callosal communication fibers or structural deformation of CC, as shown in Fig. 5, Supplementary Fig. 1, and Supplementary Animation 1. Similarly, MSA patients, particularly MSA-C types, exhibit fewer streamlines in the MCP pathway, likely due to the degeneration of pontocerebellar neurons that connect the pons to the cerebellum, a key marker differentiating MSA-C from the other, as shown in Fig. 5 and Supplementary Animation 2. Additionally, PSP and MSA-P patients also exhibit reduced streamlines in the SCP pathway, which may be due to degeneration of the SCP, a common hallmark of PSP, as shown in Fig. 5 and Supplementary Animation 3.

After exploring microstructural changes within each disease group, classification was also performed using a balanced logistic regression with complementarily paired features from specific brain regions. As shown by the marked cells in Table 2 (yellow indicating decreasing values and blue indicating increasing values), this approach enabled superior differentiation of disease groups compared to single-metric models, as shown in Fig. 6. The selection of regional diffusion metrics was performed automatically based on statistical significance (lowest p-values) and AUC (highest) values, followed by an evaluation of the complementarity behavior between features

Tissue	PD	PSP	MSA	Kruskal–Wallis		PD vs APD	PD *vs.* PSP	PD *vs.* MSA	PSP *vs.* MSA
				χ^2	*P*	*P*	post-hoc (*P*)		
MD (in $\mu m^2/s$)									
Whole brain	1160 ± 92	1200 ± 62	1195 ± 78	4.4	0.11	**0.04***(+)	0.06	0.11	0.64
White matter	866 ± 54	912 ± 49	886 ± 48	9.1	**0.011***	**0.01***(+)	**0.004***(+)	0.12	0.084
CWM	731 ± 40	778 ± 51	887 ± 161	38.4	**< 10^{-4}*****	**< 10^{-4}*****(+)	**0.0014***(+)	**< 10^{-4}*****(+)	**0.003***
CC	1123 ± 138	1258 ± 144	1154 ± 132	10.9	**0.004***	**0.027***(+)	**0.0014***(+)	0.40	0.013
Striatum	1165 ± 142	1294 ± 103	1237 ± 115	14.2	**0.0008****	**0.0007****(+)	**0.0003****(+)	0.024	0.11
GP	732 ± 86	719 ± 79	705 ± 61	0.61	0.74	0.59	0.92	0.48	0.55
SN	776 ± 113	763 ± 86	797 ± 89	2.8	0.25	0.31	0.88	0.12	0.21
RN	830 ± 102	911 ± 142	965 ± 172	18.6	**< 10^{-4}*****	**< 10^{-4}*****(+)	0.02	**< 10^{-4}*****(+)	0.2
CN	1474 ± 232	1747 ± 198	1625 ± 220	17.9	**0.0001****	**0.0002****(+)	**< 10^{-4}*****(+)	0.009	0.05
Hippocampus	1208 ± 220	1461 ± 272	1264 ± 218	13.0	**0.002***	**0.008***(+)	**0.0006****(+)	0.17	0.010
Putamen	764 ± 119	761 ± 44	766 ± 65	3.0	0.22	0.10	0.12	0.20	0.66
Thalamus	953 ± 113	1016 ± 86	996 ± 104	8.2	**0.02***	**0.006***(+)	**0.008***(+)	0.04	0.47
FA (in a.u)									
Whole brain	0.237 ± 0.012	0.225 ± 0.008	0.232 ± 0.011	14.9	**0.0006****	**0.002***(−)	**0.0003****	0.06	0.013
White matter	0.342 ± 0.018	0.323 ± 0.015	0.339 ± 0.017	13.2	**0.001***	**0.03***(−)	**0.0008***(−)	0.40	**0.002***(+)
CWM	0.391 ± 0.020	0.375 ± 0.025	0.321 ± 0.052	44.5	**< 10^{-4}*****	**< 10^{-4}*****(-)	0.15	**< 10^{-4}*****(-)	**< 10^{-4}*****(-)
CC	0.515 ± 0.065	0.432 ± 0.069	0.509 ± 0.063	16.8	**0.0002****	**0.023***(−)	**0.0002****(-)	0.55	**0.0004****(+)
Striatum	0.209 ± 0.023	0.223 ± 0.013	0.229 ± 0.019	16.3	**0.0003****	**0.0001****(+)	0.012	**0.0002****	0.17
GP	0.337 ± 0.050	0.330 ± 0.052	0.365 ± 0.048	7.4	**0.03***	0.27	0.42	0.03	0.017
SN	0.385 ± 0.053	0.433 ± 0.082	0.363 ± 0.050	12.3	**0.002***	0.78	0.02	0.05	**0.0014***
RN	0.355 ± 0.043	0.368 ± 0.050	0.347 ± 0.044	2.5	0.30	0.91	0.37	0.43	0.12
CN	0.160 ± 0.013	0.158 ± 0.010	0.157 ± 0.013	1.5	0.47	0.24	0.43	0.27	0.60
Hippocampus	0.166 ± 0.021	0.151 ± 0.012	0.166 ± 0.018	10.7	**0.005***	0.20	**0.004***(−)	0.87	**0.003***(+)
Putamen	0.249 ± 0.036	0.280 ± 0.025	0.297 ± 0.036	27.5	**< 10^{-4}*****	**< 10^{-4}*****(+)	**0.0014***(+)	**< 10^{-4}*****(+)	0.05
Thalamus	0.284 ± 0.021	0.307 ± 0.030	0.283 ± 0.016	13.2	**0.001***	0.2	**0.001***(+)	0.70	**0.001***(−)

	PD	MSA-P	MSA-C	Kruskal–Wallis		PD *vs.* MSA-P	PD *vs.* MSA-C	MSA-P *vs.* MSA-C
				χ^2	*P*	post-hoc (*P*)		
MD (in $\mu m^2/s$)								
Whole brain	1160 ± 92	1147 ± 70	1165 ± 89	0.2	0.92	0.8	0.86	0.64
White matter	866 ± 54	867 ± 41	865 ± 45	0.1	0.97	0.82	0.96	0.89
CWM	731 ± 40	796 ± 80	899 ± 108	29.1	**< 10^{-4}***	**0.006***(+)	**< 10^{-4}*****(+)	0.03(+)
CC	1123 ± 138	1149 ± 155	1070 ± 110	1.7	0.43	0.79	0.23	0.31
Striatum	1165 ± 142	1227 ± 95	1157 ± 118	2.7	0.26	0.11	0.81	0.22
GP	732 ± 86	727 ± 54	680 ± 53	3.8	0.15	0.66	0.11	0.05
SN	776 ± 113	810 ± 95	768 ± 80	2.8	0.25	0.12	0.91	0.15
RN	830 ± 102	871 ± 88	909 ± 94	9.5	**0.009***	0.09	**0.004***(+)	0.40
CN	1474 ± 233	1559 ± 180	1485 ± 217	1.5	0.48	0.22	0.96	0.43
Hippocampus	1208 ± 220	1219 ± 183	1151 ± 132	0.7	0.71	0.66	0.69	0.31
Putamen	764 ± 119	819 ± 66	734 ± 40	10.2	**0.006***	**0.004***(+)	0.83	**0.003*(-)**
Thalamus	953 ± 113	966 ± 93	939 ± 94	0.9	0.65	0.48	0.78	0.34
FA (in a.u)								
Whole brain	0.237 ± 0.012	0.235 ± 0.009	0.236 ± 0.011	0.5	0.77	0.48	0.72	0.89
White matter	0.342 ± 0.018	0.341 ± 0.013	0.346 ± 0.015	0.8	0.67	0.75	0.46	0.43
CWM	0.391 ± 0.020	0.351 ± 0.034	0.317 ± 0.038	33.6	**< 10^{-4}***	0.0004**(-)	**< 10^{-4}*****(-)	0.03
CC	0.515 ± 0.065	0.501 ± 0.061	0.541 ± 0.052	2.8	0.25	0.39	0.27	0.09
Striatum	0.209 ± 0.023	0.232 ± 0.022	0.221 ± 0.017	11.6	**0.003***	**0.001***	0.12	0.07
GP	0.337 ± 0.050	0.374 ± 0.060	0.365 ± 0.044	5.0	0.08	0.06	0.11	0.72
SN	0.385 ± 0.053	0.348 ± 0.055	0.374 ± 0.047	4.6	0.10	0.03	0.45	0.27
RN	0.355 ± 0.043	0.354 ± 0.037	0.349 ± 0.039	0.14	0.94	0.92	0.72	0.85
CN	0.160 ± 0.013	0.158 ± 0.011	0.159 ± 0.014	0.7	0.71	0.61	0.44	0.81
Hippocampus	0.166 ± 0.021	0.165 ± 0.019	0.172 ± 0.012	2.4	0.30	0.89	0.13	0.24

Continued

	PD	MSA-P	MSA-C	Kruskal–Wallis		PD *vs.* MSA-P	PD *vs.* MSA-C	MSA-P *vs.* MSA-C	
				χ^2	*P*	post-hoc (*P*)			
Putamen	0.249 ± 0.036	0.305 ± 0.040	0.277 ± 0.026	18.2	**0.0001****	**0.0002**(+)**	0.011	0.05	
Thalamus	0.284 ± 0.021	0.280 ± 0.013	0.286 ± 0.019	2.0	0.37	0.15	0.75	0.40	
	PSP	**MSA-P**	**MSA-C**	**Kruskal–Wallis**		**PSP *vs.* MSA-P**	**PSP *vs.* MSA-C**		
				χ^2	*P*	post-hoc (*P*)			
MD (in $\mu m^2/s$)									
Whole brain	1200 ± 62	1147 ± 70	1165 ± 89	4.3	0.12	0.04	0.22		
White matter	912 ± 49	867 ± 41	865 ± 45	8.3	**0.02***	0.023(−)	0.014(−)		
CWM	778 ± 51	796 ± 80	899 ± 108	12.9	**0.0016***	0.80	**0.0002****(+)		
CC	1258 ± 144	1149 ± 155	1070 ± 110	11.6	**0.003***	0.05	**0.0009****(−)		
Striatum	1294 ± 103	1227 ± 95	1157 ± 118	9.5	**0.009***	0.07	**0.004***(−)		
GP	719 ± 79	727 ± 54	680 ± 53	3.8	0.15	0.83	0.15		
SN	763 ± 86	810 ± 95	768 ± 80	2.6	0.3	0.17	0.84		
RN	911 ± 142	871 ± 88	909 ± 94	0.7	0.7	0.63	0.73		
CN	1747 ± 198	1559 ± 180	1485 ± 217	10.6	**0.005***	0.02	**0.004***(−)		
Hippocampus	1461 ± 272	1219 ± 183	1151 ± 132	12.7	**0.002***	0.015	**0.001***(−)		
Putamen	761 ± 44	819 ± 66	734 ± 40	11.2	**0.004***	0.028(+)	0.68		
Thalamus	1016 ± 86	966 ± 93	939 ± 94	5.5	0.07	0.2	0.03		
FA (in a.u)									
Whole brain	0.225 ± 0.008	0.235 ± 0.009	0.236 ± 0.011	12.4	**0.002***	**0.004***(+)	**0.003***(+)		
White matter	0.323 ± 0.015	0.341 ± 0.013	0.346 ± 0.015	14.8	**0.0006****	**0.005*(+)**	**0.0007****(+)		
CWM	0.375 ± 0.025	0.351 ± 0.034	0.317 ± 0.038	17.0	**0.0002****	0.07	**$< 10^{-4}$***(-)**		
CC	0.432 ± 0.069	0.501 ± 0.061	0.541 ± 0.052	17.3	**0.0002****	0.012	**0.0001**(+)**		
Striatum	0.223 ± 0.013	0.232 ± 0.022	0.221 ± 0.017	4.6	0.10	0.07	0.70		
GP	0.330 ± 0.052	0.374 ± 0.060	0.365 ± 0.044	5.5	0.07	0.06	0.05		
SN	0.433 ± 0.082	0.348 ± 0.055	0.374 ± 0.047	9.9	**0.007***	**0.005***(−)	0.03		
RN	0.368 ± 0.050	0.354 ± 0.037	0.349 ± 0.039	1.6	0.46	0.38	0.26		
CN	0.158 ± 0.010	0.158 ± 0.011	0.159 ± 0.014	0.2	0.89	0.77	0.65		
Hippocampus	0.151 ± 0.012	0.165 ± 0.019	0.172 ± 0.012	14.8	**0.0006****	0.03	**0.0002****(+)		
Putamen	0.280 ± 0.025	0.305 ± 0.040	0.277 ± 0.026	6.0	0.051	0.02	0.81		
Thalamus	0.307 ± 0.030	0.280 ± 0.013	0.286 ± 0.019	10.4	**0.006***	**0.003*(-)**	0.03		

Table 2. Statistical and ROC curve analysis using MD (in $\mu m^2/s$) and FA (in a.u) of brain tissues to differentiate PD, PSP, and MSA as well as MSA subtypes. Data are shown as the mean ± standard deviation. Post hoc (*p*): *p* values from post hoc analysis of the Mann–Whitney U test. *: $p < 0.05$, **: $p < 0.001$ and ***: $p < 10^{-4}$. (For post hoc analysis: *: $p < 0.05$, **: $p < 0.001$, and ***: $p < 10^{-4}$ after Bonferroni correction). The significant *p*-values are displayed in bold. The marked cells in each binary comparison represent the pair of asymmetric diffusion metrics and brain tissues used for enhancing the differentiation of groups. The signs (+ and -) indicate increasing or decreasing metrics.

for each disease pair comparison. Figure 6 summarizes the differentiation accuracy, sensitivity, and AUC values for each two-class comparison based on paired asymmetric diffusion metrics.

Notably, with four-fold cross-validation, PD and PSP were differentiated using a combination of low FA in the CC and high MD in the caudate nucleus, yielding an average accuracy, sensitivity, and F1-score values of 0.72, 0.71 and 0.69, respectively using Logistic regression. The ROC curve analysis also yielded an average AUC of 0.83 (95% confidence interval (CI): 0.53–0.97). To differentiate PD and MSA, a combination of low FA in the CWM and high FA in the putamen achieved average accuracy, sensitivity, and F1-score of 0.89 each, as well as an average AUC of 0.98(95% CI: 0.84 -1.0). In distinguishing PSP and MSA, an average accuracy of 0.76, sensitivity of 0.77, F1-score of 0.75, and AUC of 0.87 (95% CI: 0.54–0.99) were obtained using low FA in the CWM and high FA in the CC. Similarly, PD and atypical Parkinsonian syndromes were also classified using low FA of the CWM and high FA of the putamen. The classification achieved an average accuracy of 0.79, sensitivity of 0.78, F1-score of 0.78, and AUC of 0.92 (95% CI: 0.69–0.97), as shown in Fig. 6. Similarly, the discrimination of MSA-P and MSA-C subtypes yielded an average accuracy of 0.72, a sensitivity of 0.73, F1-score of 0.72, and AUC of 0.83(95% CI: 0.49–0.98), using high MD in CWM and low MD in putamen.

Distinguishing between MSA, particularly the MSA-P subtype with PD and PSP, using two asymmetric diffusion metrics, remains challenging. This difficulty is consistent with the low statistical significance observed in comparing MSA-P with PD as well as PSP reported in Table 2. Notably, reducing the sixty diffusion features

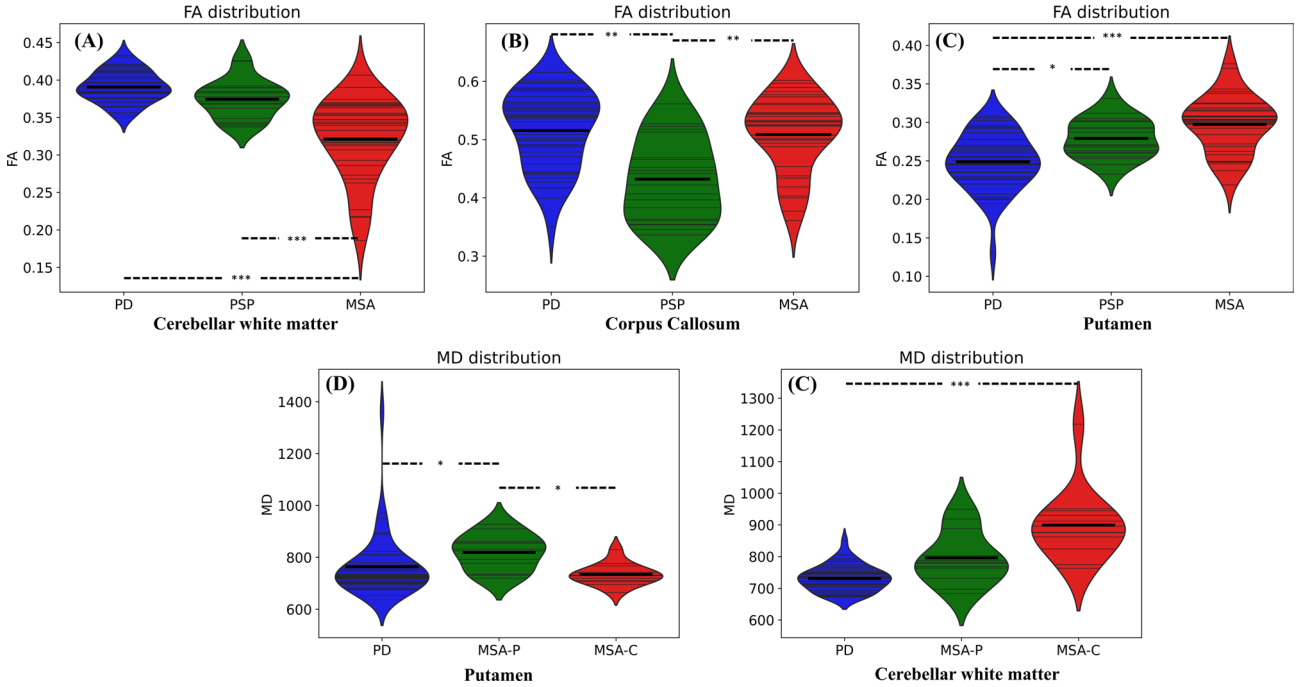

Fig. 4. Violin plots of diffusion metrics in selected brain regions with strong discriminative power. *: $p < 0.05$, **: $p < 0.001$, and ***: $p < 10^{-4}$ using Mann–Whitney U test after Bonferroni correction. A-E represent optimal biomarkers for MSA, PSP, PD, MSA-P, and MSA-C groups, respectively.

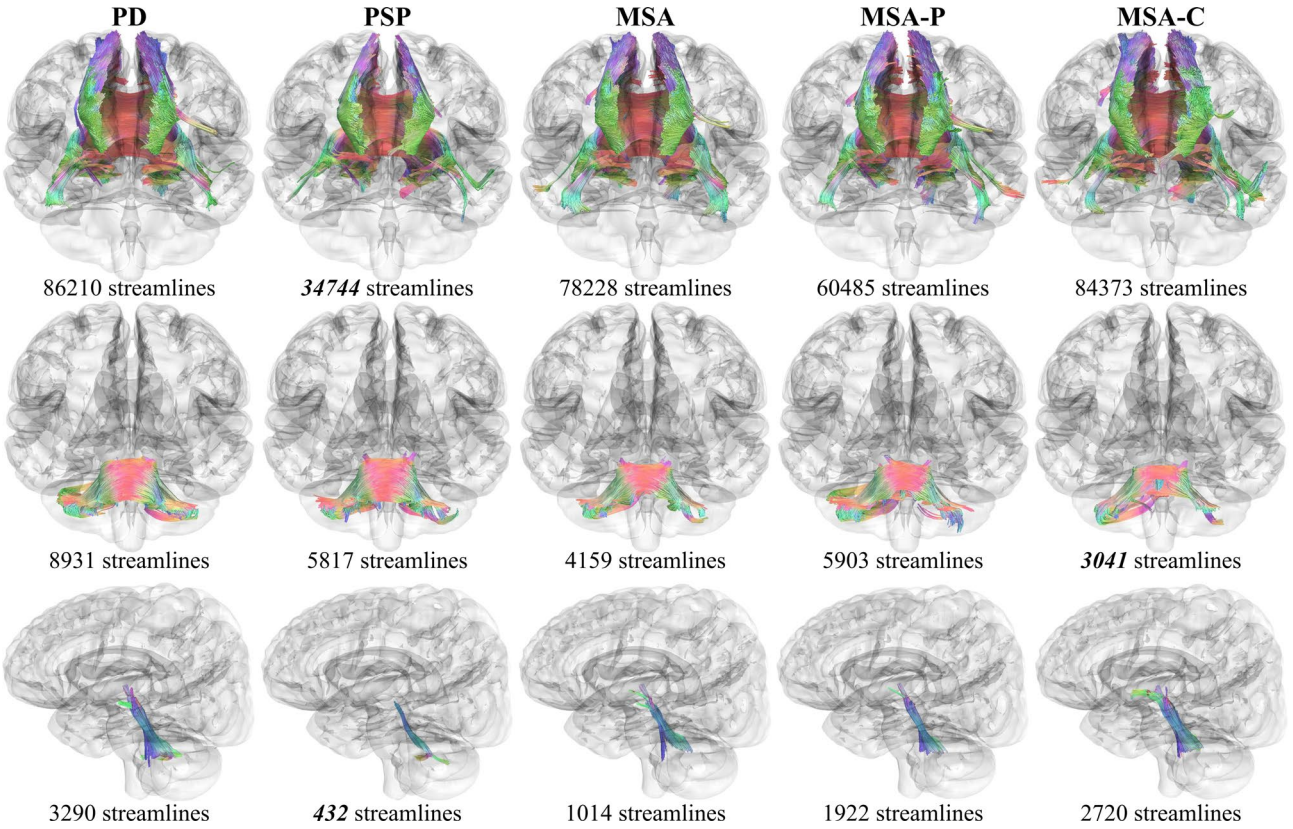

Fig. 5. Group-level comparison using disease-specific neuronal pathways. The first, second, and third rows show the callosal, MCP, and SCP pathways, respectively, using deterministic fiber tracking. Deterministic tractography was performed on group-averaged diffusion data, and disease-specific neuronal fibers were extracted using the auto-track function in DSI Studio for group-level visualization and comparison.

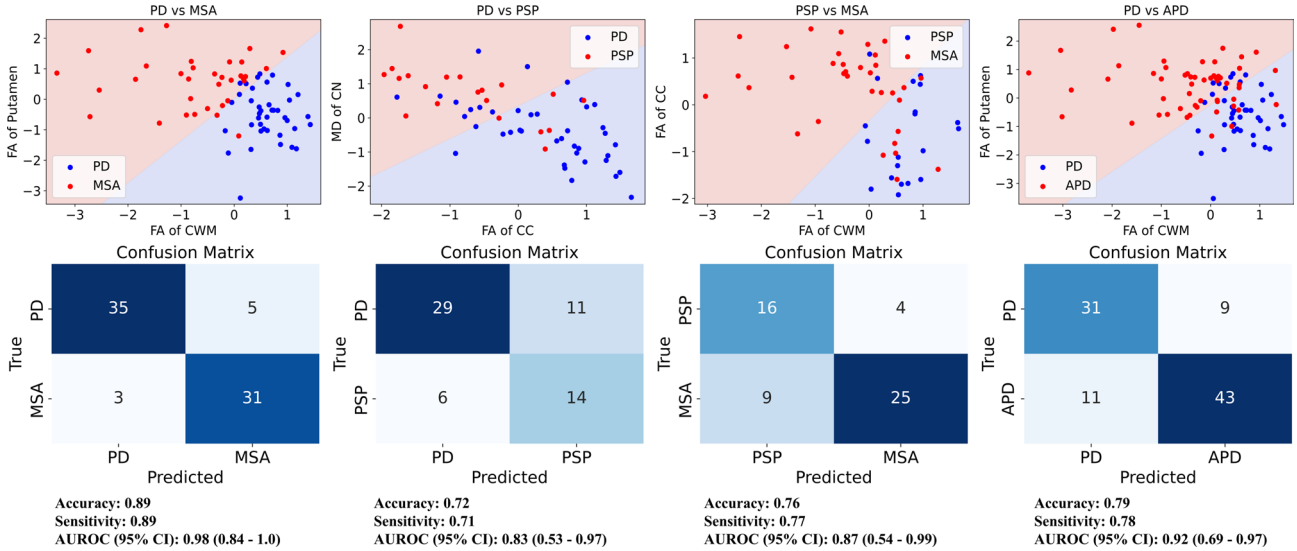

Fig. 6. Classification for disease differentiation. The top row shows the data distribution and the decision boundaries of the logistic regression classifier using two strategically selected asymmetric diffusion metrics, visualized in two-dimensional feature space. The bottom row shows classification performance summarized by confusion matrices obtained from four-fold cross-validation. CI: confidence interval.

of every subject to orthogonal components via PCA did not appear to significantly enhance classification performance. As shown in Supplementary Fig. 2, multivariable logistic regression using the first seven PCs produced AUC values comparable to those obtained only with the two complementarily paired metrics. Supplementary Fig. 2 also illustrates a general trend of differentiability with increasing numbers of PCs up to approximately 83% explained variance. However, the lack of significant AUC improvement with PCA suggests that most of the variance relevant for classification is mostly captured by the two selected asymmetric diffusion metrics.

Discussion and conclusion

Over the past few decades, MRI has yielded many biomarkers for differentiating Parkinsonian disorders. Early work emphasized macroscopic features such as regional atrophy, structural deformation, and iron deposition to separate disease subtypes[21]. DTI then supplemented these approaches, revealing region-specific water-diffusion abnormalities that reliably distinguish PD, PSP, and MSA[3,31]. Recent large-cohort machine-learning studies report that diffusion-based microstructural metrics can offer even greater discriminative power across Parkinsonian syndromes[3]. Although diffusion abnormalities are spatially heterogeneous and pathway-specific, high-dimensional classifiers need large sample sizes. Therefore, we use a compact set of complementarily distributed diffusion metrics from key regions that mechanistically differentiate PD, PSP, and MSA, providing interpretable and clinically practical results even with limited data.

In patients with PD, despite notable inconsistencies across studies, DTI has shown reduced FA and increased diffusivity (MD, AD, and RD) measures primarily in the SN and putamen[31,47]. These changes are thought to reflect the degeneration of dopaminergic neurons. In PSP, significant reductions in FA and increases in MD, RD, and AD have been reported, particularly in the SCP, CC, and midbrain[4,48,49]. These findings are associated with midbrain atrophy, a well-established imaging marker used to distinguish PSP from other Parkinsonian syndromes. MSA, especially MSA-C, exhibits distinct DTI patterns, including increased MD and reduced FA in the MCP, cerebellum, and pons due to degeneration of afferent fibers connecting the cerebellum and pons[11,18,33]. Our diffusion metrics not only support previously reported alterations of diffusion metrics[18] but also demonstrate that regionally asymmetric changes can complementarily differentiate Parkinsonian syndromes. Specifically, elevated FA in the putamen combined with reduced FA in CWM distinguishes MSA from PD, achieving a four-fold cross-validated AUROC of 0.98. For PSP versus PD, higher MD in caudate nucleus coupled with lower FA in CC yielded an AUROC of 0.83. Increased FA in the CC alongside decreased CWM FA separates MSA from PSP, with an AUROC of 0.87. We observed lower classification performance especially between MSA-P compared with PSP and PD, likely due to overlapping microstructural alterations[50]. This is supported by the relatively large p-values in Table 2 for this comparison, in contrast to the clearer separations observed in other group pairs.

Although limited in some aspects, DTI-based fiber tractography has been increasingly applied to the study of neurodegeneration, offering a more targeted approach for investigating the degeneration of specific neural pathways[36]. In particular, analysis of the MCP has been used to differentiate MSA patients from both healthy controls and those with PD, with tractography revealing significant alterations in the MSA group[51]. Consistent with these findings, our results also indicate notable degeneration of the MCP in MSA patients, as demonstrated through deterministic tractography. Similarly, degeneration of the SCP, as well as corpus callosal pathways,

are widely reported in PSP patients[52], which is also supported by our findings. On the other hand, similar degeneration of SCP was also observed in MSA-P patients in this study.

Consistent with prior research studies in the field[21,50,53–55], a key limitation was the relatively small sample size, an inherent reflection of the rarity of atypical Parkinsonian syndromes. This underscores the need for continued research and multi-center collaboration to further validate and extend these findings. While this limitation affects statistical power and constrains the use of machine learning-based classification models, the use of age- and gender-balanced cohorts remain well-suited for investigating the mechanistic basis of group discriminability. Although not optimal for training robust predictive models, this age- and gender-matched sample registered to a locally designed, population-specific template allows for statistically controlled comparisons and more precise interpretation of region-specific diffusion alterations underlying disease differentiation, an approach particularly valuable for modest clinical cohorts encountered in routine practice. In addition, even though k-fold cross-validation was employed to enhance generalizability, validating the method on an independent dataset would provide stronger evidence of its robustness. This can be achieved in future work through collaborations with multiple centers utilizing multi-vendor scanners and including diverse patient demographics not only different disease subtypes but also age- and gender-matched healthy control datasets which is one of our main future objectives. Access to a larger and more heterogeneous dataset will further enable the incorporation of additional tissue and diffusion features without increasing the risk of model overfitting. Another key limitation lies in the use of low-resolution T_2-weighted(b_0) images for DBM analysis. Although higher-resolution imaging could potentially yield more accurate DBM results, employing a single imaging protocol allows for a more streamlined and cost-effective approach that reduces scan time and patient burden. Additionally, this study included only disease groups and did not incorporate a healthy control group. While comparisons between diseased groups and healthy controls are relatively straightforward, distinguishing among different Parkinsonian syndromes is inherently more complex and clinically relevant. Future studies should aim to address these limitations by incorporating larger cohorts, using higher-resolution imaging when feasible, and adopting more accurate, objective and reproducible methods for tissue masking and fiber tracking. These improvements could significantly enhance the accuracy and reliability of disease differentiation. In addition, combining diffusion metrics with iron-sensitive or neuromelanin-sensitive MRI could potentially enhance diagnostic accuracy in future studies[56,57].

In conclusion, our DTI-based analyses, including diffusivity measures and tractography, consistently revealed significant degeneration of the MCP in MSA patients, as well as the SCP and callosal pathways in PSP patients. In contrast, PD patients exhibited notable alterations primarily in the putamen compared to the other groups. Furthermore, integrating two systematically selected complementarily paired diffusion metrics from different brain regions improves discriminative power compared to individual metrics and provides a more human-interpretable decision boundary for differential diagnosis, enabling deeper insight into the distinct pathologies of PD, PSP, and MSA.

Data availability

The datasets generated or analyzed during this study are available from the corresponding author upon reasonable request.

Received: 11 August 2025; Accepted: 23 February 2026
Published online: 03 March 2026

References

1. Jankovic, J. Parkinson's disease: Clinical features and diagnosis. *J. Neurol. Neurosurg. Psychiatry* **79**(4), 368–376. https://doi.org/10.1136/jnnp.2007.131045 (2008).
2. Mcfarland, N. R. Diagnostic approach to atypical Parkinsonian syndromes. *Contin. Lifelong Learn. Neurol.* **22**(4 Movement Disorders), 1117. https://doi.org/10.1212/CON.0000000000000348 (2016).
3. Vaillancourt, D. E. et al. Automated imaging differentiation for parkinsonism. *JAMA Neurol.* **82**(5), 495–505. https://doi.org/10.1001/jamaneurol.2025.0112 (2025).
4. Worker, A. et al. Diffusion tensor imaging of Parkinson's disease, multiple system atrophy and progressive supranuclear palsy: A tract-based spatial statistics study. *PLoS ONE* https://doi.org/10.1371/journal.pone.0112638 (2014).
5. Bergamino, M., Keeling, E. G., Mishra, V. R., Stokes, A. M. & Walsh, R. R. Assessing white matter pathology in early-stage parkinson disease using diffusion mri: A systematic review. *Front. Neurol.* **11**, 522616. https://doi.org/10.3389/FNEUR.2020.00314/BIBTEX (2020).
6. Paviour, D., Price, S. L., Jahanshahi, M., Lees, A. J. & Fox, N. C. Regional brain volumes distinguish PSP, MSA-P, and PD: MRI-based clinico-radiological correlations. *Mov Disord.* **21**(7), 989–996. https://doi.org/10.1002/MDS.20877 (2006).
7. Josephs, K. A. et al. Modeling trajectories of regional volume loss in progressive supranuclear palsy. *Mov Disord.* **28**(8), 1117–1124. https://doi.org/10.1002/MDS.25437 (2013).
8. Potrusil, T. et al. Diagnostic potential of automated tractography in progressive supranuclear palsy variants. *Parkinsonism Relat. Disord.* **72**, 65–71. https://doi.org/10.1016/j.parkreldis.2020.02.007 (2020).
9. DeRosier, F. et al. Progressive supranuclear palsy: Neuropathology, clinical presentation, diagnostic challenges, management, and emerging therapies. *Dis. Mon.* **70**(8), 101753. https://doi.org/10.1016/j.disamonth.2024.101753 (2024).
10. Tessema, A. W. et al. Automated volumetric determination of high R2* regions in substantia nigra: A feasibility study of quantifying substantia nigra atrophy in progressive supranuclear palsy. *NMR Biomed.* **35**(11), e4795. https://doi.org/10.1002/NBM.4795 (2022).
11. Yang, H. G. et al. Cerebellar atrophy and its contribution to motor and cognitive performance in multiple system atrophy. *NeuroImage: Clinical* **23**, 101891. https://doi.org/10.1016/J.NICL.2019.101891 (2019).
12. Liu, M., Wang, Z. & Shang, H. Multiple system atrophy: An update and emerging directions of biomarkers and clinical trials. *J. Neurol.* **271**(5), 2324–2344. https://doi.org/10.1007/S00415-024-12269-5/TABLES/1 (2024).
13. Grimm, M. J. et al. Clinical conditions "suggestive of progressive supranuclear palsy"—diagnostic performance. *Mov. Disord.* **35**(12), 2301–2313. https://doi.org/10.1002/mds.28263 (2020).

14. Koga, S. et al. When DLB, PD, and PSP masquerade as MSA. *Neurology* **85**(5), 404–412. https://doi.org/10.1212/WNL.0000000000001807 (2015).
15. Miki, Y. et al. Identification of multiple system atrophy mimicking Parkinson's disease or progressive supranuclear palsy. *Brain* **144**(4), 1138–1151. https://doi.org/10.1093/brain/awab017 (2021).
16. Morelli, M. et al. Accuracy of magnetic resonance parkinsonism index for differentiation of progressive supranuclear palsy from probable or possible Parkinson disease. *Mov. Disord.* **26**(3), 527–533. https://doi.org/10.1002/MDS.23529 (2011).
17. Constantinides, V. C., Paraskevas, G. P., Stamboulis, E. & Kapaki, E. Simple linear brainstem MRI measurements in the differential diagnosis of progressive supranuclear palsy from the parkinsonian variant of multiple system atrophy. *Neurol. Sci.* **39**(2), 359–364. https://doi.org/10.1007/S10072-017-3212-2 (2018).
18. Ramli, N., Nair, S. R., Ramli, N. M. & Lim, S. Y. Differentiating multiple-system atrophy from Parkinson's disease. *Clin. Radiol.* **70**(5), 555–564. https://doi.org/10.1016/j.crad.2015.01.005 (2015).
19. Trujillo, P., Aumann, M. A. & Claassen, D. O. Neuromelanin-sensitive MRI as a promising biomarker of catecholamine function. *Brain* **147**(2), 337–351. https://doi.org/10.1093/brain/awad300 (2024).
20. Cao, Q. et al. Diagnostic value of combined magnetic resonance imaging techniques in the evaluation of Parkinson disease. *Quant Imaging Med Surg.* **13**(10), 6503–6516. https://doi.org/10.21037/QIMS-23-87/COIF (2023).
21. Li, Y. et al. The value of quantitative susceptibility mapping and morphometry in the differential diagnosis of Parkinsonism. *Am. J. Neuroradiol.* **46**(7), ajnr.A8665. https://doi.org/10.3174/ajnr.a8665 (2025).
22. Huppertz, H. J. et al. Differentiation of neurodegenerative parkinsonian syndromes by volumetric magnetic resonance imaging analysis and support vector machine classification. *Mov. Disord.* **31**(10), 1506–1517. https://doi.org/10.1002/MDS.26715 (2016).
23. Ito, S., Makino, T., Shirai, W. & Hattori, T. Diffusion tensor analysis of corpus callosum in progressive supranuclear palsy. *Neuroradiology* **50**(11), 981–985. https://doi.org/10.1007/S00234-008-0447-X (2008).
24. Eugenia Caligiuri, M. et al. Corpus callosum damage in PSP and unsteady PD patients: A multimodal MRI study. *Neuroimage (Amst)* **43**, 103642. https://doi.org/10.1016/J.NICL.2024.103642 (2024).
25. Padovani, A., Borroni, B. & Brambati, S. M. Diffusion tensor imaging and voxel based morphometry study in early progressive supranuclear palsy. *J. Neurol. Neurosurg. Psychiatry* **77**(4), 457–463. https://doi.org/10.1136/JNNP.2005.075713 (2006).
26. Massey, L. A. et al. Conventional magnetic resonance imaging in confirmed progressive supranuclear palsy and multiple system atrophy. *Mov. Disord.* **27**(14), 1754–1762. https://doi.org/10.1002/MDS.24968 (2012).
27. Lee, J. H. & Lee, M. S. Brain iron accumulation in atypical parkinsonian syndromes: In vivo MRI evidences for distinctive patterns. *Front. Neurol.* **10**, 74. https://doi.org/10.3389/FNEUR.2019.00074/FULL (2019).
28. Minati, L. & Weglarz, W. P. Physical foundations, models, and methods of diffusion magnetic resonance imaging of the brain: A review. *Concepts Magn. Reson. Part A Bridg. Educ. Res.* **30**(5), 278–307. https://doi.org/10.1002/CMR.A.20094 (2007).
29. Mukherjee, P., Berman, J. I., Chung, S. W., Hess, C. P. & Henry, R. G. Diffusion tensor MR imaging and fiber tractography: Theoretic underpinnings. *AJNR Am. J. Neuroradiol.* **29**(4), 632–641. https://doi.org/10.3174/AJNR.A1051 (2008).
30. Xu, C., Neuroth, T., Fujiwara, T., Liang, R. & Ma, K. L. A predictive visual analytics system for studying neurodegenerative disease based on DTI fiber tracts. *IEEE Trans. Vis. Comput. Graph.* **29**(4), 2020–2035. https://doi.org/10.1109/TVCG.2021.3137174 (2023).
31. Zhang, Y. & Burock, M. A. Diffusion tensor imaging in Parkinson's disease and Parkinsonian syndrome: A systematic review. *Front. Neurol.* **11**, 531993. https://doi.org/10.3389/FNEUR.2020.531993/PDF (2020).
32. Krismer, F. et al. Automated analysis of diffusion-weighted magnetic resonance imaging for the differential diagnosis of multiple system atrophy from Parkinson's disease. *Mov Disord* **36**(1), 241–245. https://doi.org/10.1002/MDS.28281 (2021).
33. Pasquini, J., Firbank, M. J., Ceravolo, R., Silani, V. & Pavese, N. Diffusion magnetic resonance imaging microstructural abnormalities in multiple system atrophy: A comprehensive review. *Mov. Disord.* **37**(10), 1963–1984. https://doi.org/10.1002/MDS.29195 (2022).
34. Tir, M., Delmaire, C., Besson, P. & Defebvre, L. The value of novel MRI techniques in Parkinson-plus syndromes: Diffusion tensor imaging and anatomical connectivity studies. *Rev. Neurol. (Paris)* **170**(4), 266–276. https://doi.org/10.1016/J.NEUROL.2013.10.013 (2014).
35. Nigro, P. et al. Changes of olfactory tract in Parkinson's disease: a DTI tractography study. *Neuroradiology* **63**(2), 235–242. https://doi.org/10.1007/S00234-020-02551-4/FIGURES/3 (2021).
36. Zhang, Y. et al. Diffusion tensor imaging of the nigrostriatal fibers in Parkinson's disease. *Mov. Disord.* **30**(9), 1229–1236. https://doi.org/10.1002/MDS.26251 (2015).
37. Shih, Y. C., Tseng, W. Y. I. & Montaser-Kouhsari, L. Recent advances in using diffusion tensor imaging to study white matter alterations in Parkinson's disease: A mini review. *Front. Aging Neurosci.* **14**, 1018017. https://doi.org/10.3389/FNAGI.2022.1018017/BIBTEX (2022).
38. Abos, A. et al. Differentiation of multiple system atrophy from Parkinson's disease by structural connectivity derived from probabilistic tractography. *Sci. Rep.* https://doi.org/10.1038/S41598-019-52829-8 (2019).
39. Hughes, A. J., Daniel, S. E., Kilford, L. & Lees, A. J. Accuracy of clinical diagnosis of idiopathic Parkinson's disease: A clinico-pathological study of 100 cases. *J. Neurol. Neurosurg. Psychiatry* **55**(3), 181–184. https://doi.org/10.1136/JNNP.55.3.181 (1992).
40. Gilman, S. et al. Second consensus statement on the diagnosis of multiple system atrophy. *Neurology* **71**(9), 670–676. https://doi.org/10.1212/01.WNL.0000324625.00404.15/ASSET/1A9D1BEF-C398-4065-A39A-E91F747F8607/ASSETS/GRAPHIC/11FSM1.GIF (2008).
41. Höglinger, G. U. et al. Clinical diagnosis of progressive supranuclear palsy: The movement disorder society criteria. *Mov. Disord.* **32**(6), 853–864. https://doi.org/10.1002/MDS.26987 (2017).
42. Yeh, F. C., Wedeen, V. J. & Tseng, W. Y. I. Generalized q-sampling imaging. *IEEE Trans. Med. Imaging* **29**(9), 1626–1635. https://doi.org/10.1109/TMI.2010.2045126 (2010).
43. Basser, P. J. & Jones, D. K. Diffusion-tensor MRI: Theory, experimental design and data analysis - A technical review. *NMR Biomed.* **15**(7–8), 456–467. https://doi.org/10.1002/nbm.783 (2002).
44. Yeh, F. C., Verstynen, T. D., Wang, Y., Fernández-Miranda, J. C. & Tseng, W. Y. I. Deterministic diffusion fiber tracking improved by quantitative anisotropy. *PLoS ONE* **8**(11), e80713. https://doi.org/10.1371/JOURNAL.PONE.0080713 (2013).
45. Yeh, F. C. et al. Automatic removal of false connections in Diffusion MRI tractography using Topology-Informed Pruning (TIP). *Neurotherapeutics* **16**(1), 52–58. https://doi.org/10.1007/S13311-018-0663-Y (2019).
46. Mazziotta, J. C., Toga, A. W., Evans, A., Fox, P. & Lancaster, J. A probabilistic atlas of the human brain: Theory and rationale for its development. *Neuroimage* **2**(2), 89–101. https://doi.org/10.1006/nimg.1995.1012 (1995).
47. Deng, X. Y., Wang, L., Yang, T. T., Li, R. & Yu, G. A meta-analysis of diffusion tensor imaging of substantia nigra in patients with Parkinson's disease. *Sci. Rep.* **8**(1), 1–8. https://doi.org/10.1038/s41598-018-20076-y (2018).
48. Saini, J. et al. In vivo evaluation of white matter pathology in patients of progressive supranuclear palsy using TBSS. *Neuroradiology* **54**(7), 771–780. https://doi.org/10.1007/S00234-011-0983-7 (2012).
49. Rosskopf, J. et al. Frontal corpus callosum alterations in progressive supranuclear palsy but not in Parkinson's disease. *Neurodegener. Dis.* **14**(4), 184–193. https://doi.org/10.1159/000367693 (2014).
50. Seppi, K. et al. Diffusion-weighted imaging discriminates progressive supranuclear palsy from PD, but not from the parkinson variant of multiple system atrophy. *Neurology* **60**(6), 922–927. https://doi.org/10.1212/01.WNL.0000049911.91657.9D (2003).
51. Beliveau, V. et al. Characterization and diagnostic potential of diffusion tractography in multiple system atrophy. *Parkinsonism Relat. Disord.* **85**, 30–36. https://doi.org/10.1016/J.PARKRELDIS.2021.02.027 (2021).

52. Costa, F. et al. Longitudinal assessment of white matter alterations in progressive supranuclear palsy variants using diffusion tractography. *Parkinsonism Relat. Disord.* https://doi.org/10.1016/j.parkreldis.2025.107272 (2025).
53. Eckert, T. et al. Differentiation of idiopathic Parkinson's disease, multiple system atrophy, progressive supranuclear palsy, and healthy controls using magnetization transfer imaging. *Neuroimage* **21**(1), 229–235. https://doi.org/10.1016/j.neuroimage.2003.08.028 (2004).
54. Focke, N. K. et al. Differentiation of typical and atypical Parkinson syndromes by quantitative MR imaging. *AJNR Am. J. Neuroradiol.* **32**(11), 2087–2092. https://doi.org/10.3174/ajnr.A2865 (2011).
55. Paviour, D. C., Thornton, J. S., Lees, A. J. & Jäger, H. R. Diffusion-weighted magnetic resonance imaging differentiates parkinsonian variant of multiple-system atrophy from progressive supranuclear palsy. *Mov. Disord.* **22**(1), 68–74. https://doi.org/10.1002/mds.21204 (2007).
56. Ito, K. et al. Differential diagnosis of parkinsonism by a combined use of diffusion kurtosis imaging and quantitative susceptibility mapping. *Neuroradiology* **59**(8), 759–769. https://doi.org/10.1007/s00234-017-1870-7 (2017).
57. Andersson Forsman, O., Sjöström, H., Svenningsson, P. & Granberg, T. Combined MR quantitative susceptibility mapping and multi-shell diffusion in Parkinson's disease. *J. Neuroimaging* **34**(5), 603–611. https://doi.org/10.1111/jon.13222 (2024).

Acknowledgements

We sincerely thank the patients who participated in this study. Their generous contribution of time and effort made this research possible. We are deeply grateful for their willingness to support scientific advancement and clinical understanding through their involvement.

Author contributions

(1) Research project: A. Conceptualization, B. Organization and Planning, C. Execution; (2) Data Analysis: A. Data Collection and Labeling, B. Data Processing, C. Execution, D. Review and Critique; (3) Manuscript Preparation: A. Writing of the first draft, B. Review and Critique. C. Editing of the final version of the manuscript. A.W.T.: 1A, 1B, 1C, 2B, 2C, 3A, 3C S.J.: 2A, 2D, 3B Y.R.K.: 2A, 2D, 3B H.Y.L.: 2A, 2D, 3B G.Y.L.: 2A, 2D, 3B C.H.S.: 2A, 2D, 3B J.R.: 2A, 2D, 3B S.J.C.: 2A, 2D, 3B E.J.L.: 1A, 1B, 1C, 2A, 2B, 2C, 2D, 3B H.J.C.: 1A, 1B, 1C, 2B, 2C, 2D, 3A, 3B, 3C.

Funding

This work was partially supported by grants from the National Research Foundation of Korea of the Korean government (grant numbers: RS-2025-00559394 and RS-2025-02216928). This research was also supported by the National Research Council of Science & Technology (NST), funded by the Korean government (MSIT) (grant number: GTL25071-000). This research was also supported by grant from the Asan Institute for Life Sciences, Asan Medical Center, Seoul, Korea (grant number: 2023IP0110), University of Ulsan, and Ulsan National Institute of Science and Technology, funded by the Korean government.

Declarations

Competing interests

The authors declare no competing interests.

Additional information

Supplementary Information The online version contains supplementary material available at https://doi.org/10.1038/s41598-026-41695-w.

Correspondence and requests for materials should be addressed to E.-J.L. or H.C.

Reprints and permissions information is available at www.nature.com/reprints.

Publisher's note Springer Nature remains neutral with regard to jurisdictional claims in published maps and institutional affiliations.